Anisotropic velocity statistics of topological defects under shear flow

Luiza Angheluta,[1,2] Patricio Jeraldo,[2] and Nigel Goldenfeld[2]
[1]*Physics of Geological Processes, Department of Physics, University of Oslo, 0316 Oslo, Norway*
[2]*Loomis Laboratory of Physics, Department of Physics, University of Illinois at Urbana-Champaign, 1110 West Green Street, Urbana, Illinois 61801, USA*
(Received 24 November 2011; published 31 January 2012)

We report numerical results on the velocity statistics of topological defects during the dynamics of phase ordering and nonrelaxational evolution assisted by an external shear flow. We propose a numerically efficient tracking method for finding the position and velocity of defects and apply it to vortices in a uniform field and dislocations in anisotropic stripe patterns. During relaxational dynamics, the distribution function of the velocity fluctuations is characterized by a dynamical scaling with a scaling function that has a robust algebraic tail with an inverse cube power law. This is characteristic of defects of codimension 2, e.g., point defects in two dimensions and filaments in three dimensions, regardless of whether the motion is isotropic (as for vortices) or highly anisotropic (as for dislocations). However, the anisotropic dislocation motion leads to anisotropic statistical properties when the interaction between defects and their motion is influenced by the presence of an external shear flow transverse to the stripe orientation.

DOI: 10.1103/PhysRevE.85.011153 PACS number(s): 64.60.Bd, 61.30.Jf, 47.55.pb, 74.40.Gh

I. INTRODUCTION

The small-scale dynamics of interacting defects plays an important role in the evolution of complex systems. In particular, topological defects are a common occurrence in systems supporting a continuous symmetry that is spontaneously broken in the process of a nonequilibrium phase transition. One central question is how the universal properties and scaling laws near a critical phase transition relate to the presence and interactions of defects. The formation and evolution of topological defects are typically formulated in the framework of the Ginzburg-Landau theory of symmetry-breaking phase transitions, where defects are described as phase singularities in a complex order-parameter field (rotational symmetry) [1,2].

The equilibrium structure of isolated topological defects is deeply rooted in their topological properties and is relatively well studied and understood [2]. In contrast, the dynamical and statistical properties of interacting topological defects during a nonequilibrium phase transition are far less understood and are the subject of more recent systematic analyses. Numerous studies have focused on the statistical properties of topological defect ensembles in relation to the large-scale properties of the system. Examples include the quenching dynamics during phase-ordering kinetics [3,4], the motion of defects in convection patterns [5], the dislocation dynamics in crystal plasticity [6,7], and the vortex filament motion in quantum flows [8]. A common characteristic of these apparently disparate systems is that they support codimension-2 topological defects, that is, dislocations and vortices which in two dimensions (2D) become point defects and defect filaments or loops in three dimensions (3D). One common finding is the presence of a robust scaling law in the local velocity statistics for these kind of defects. Recent experiments on decaying quantum turbulence in ^{4}He report that the velocity field v induced by quantized vortices is characterized by a v^{-3} scaling, attributed to the rare reconnection events between vortex filaments [9] and reproduced numerically in atomic Bose-Einstein condensates [10] and counterflow turbulence [11]. Similar velocity statistics has been observed in a discrete dislocation dynamics model of crystal plasticity [12] and in experiments on thermal convection in an inclined fluid layer [13].

Theoretically, the asymptotic tail of the velocity probability distribution $P(v)$ can be calculated in a statistical formulation of random stationary configurations of point defects interacting through a logarithmic potential in 2D [6,14]. The model predicts the same tail distribution both in neutral systems (zero net topological charge) and systems with a single-charge distribution. An inverse cubic scaling is consistent with the approximation of the nearest-neighbor interaction between defects uniformly distributed in space [14]. In theoretical studies of defect motion during phase-ordering kinetics, the inverse cubic law is related to the annihilation events of defect loops or between point defects with opposite topological charges [4,15,16]. The coarsening during phase ordering is reflected in a time-dependent density of defects and their velocity distribution $F(v,t)$, which is characterized by a dynamical scaling law related to the growth law of the characteristic length scale in the ordering kinetics [15–17]. For nonconservative dynamics of the order parameter, the distribution of velocity for point defects in 2D takes the form $F(v,t) = \langle v(t)\rangle^{-1} P[v/\langle v(t)\rangle]$, where the scaling function is $P(x) \sim x(1+x^2)^{-2}$ and the ensemble average velocity $\langle v(t)\rangle$ at time t is related to the average distance between defects $L(t)$ at time t and scales with time as $\langle v(t)\rangle \sim 1/L(t) \sim t^{-1/2}$ [15,16]. A different scaling exponent for the scaling function $P(x)$ is predicted for defect filaments in 3D [4,15], whereas experiments [9] and numerics [11,12] suggest the same scaling as for point defects.

In contrast to isotropic vortex dynamics, dislocation motion in crystals, as well as in stripe patterns, is typically anisotropic when confined to certain gliding and climbing planes. In addition, dislocations often coexist and interact with other kinds of defects such as disinclinations and grain boundaries, which makes it harder to study in isolation. For this reason, phase ordering is much more difficult to study in isotropic stripe phases and polycrystalline phases than in anisotropic stripes and single crystals where only dislocations are present [18,19].

Stripe ordering is a common pattern occurring in a diversity of systems from zebra patterns to sand ripples and in classical fluid convection systems, where defects are local tears of the underlying pattern [5]. Anisotropic stripes or rolls develop by an uniaxial ordering of stripes as happens, for instance, in electrically driven convection flows of nematic liquid crystals (electrohydrodynamic convection) [20] or in thermal convection flows of isotropic fluids down an inclined plane [21].

During relaxational dynamics, where the motion of defects is dominated by mutual interactions prior to annihilations, the statistics of the velocity components keeps the same form even in the presence of strongly anisotropic motion of defects. A numerical study of 2D phase ordering after a quench from a disordered state described by a nonconservative time-dependent real Ginzburg-Landau model showed that the isotropic motion of point vortices is characterized by a statistical distribution with an inverse cubic tail in the scaling function $P(v)$, as predicted theoretically [22]. Similar statistical distributions for the climbing (motion along the direction of the stripes) and gliding (motion across the stripes) velocities of point dislocations have been reproduced in a numerical study of phase ordering in anisotropic stripes in two dimensions [23]. This is consistent with the theoretical understanding that the dislocation motion in anisotropic stripes can be in fact mapped onto a Ginzburg-Landau vortex dynamics [2]. This also means that, to the leading-order approximation, the interactions between dislocations are expected to be similar to those between vortices.

The statistics of defect motion during nonrelaxational evolution of the system, self-sustained or driven by an external field, is less well understood due to correlation effects or additional driving forces apart from the mutual nearest-neighbor interactions between defects. A self-sustained motion of defects is obtained in convection patterns when the mean flow due to vertical vorticity, driven by the undulations in the normal stripes and the presence of defects, acts as a self-induced drift in the motion of defects [24]. This nontrivial dynamics of defects leads to a spatiotemporal chaotic state also know as "defect turbulence," which was observed experimentally in fluid convection systems [21,25] or diffusion-reaction systems [26] and studied in numerous theoretical and numerical investigations [24,27–30]. In this chaotic dynamical regime, a statistically stationary distribution of the number of defects is maintained by the defect annihilations and the spontaneous creations of pairs due to the phase instability. To leading order in the approximation of well-mixed and independent defects, the distribution of the number of defects follows the Poisson statistics with mean-square fluctuations given by the mean number of defects [27]. The well-mixed assumption implies that defect pairs are being created and annihilated randomly, whereas experiments and numerical studies suggest that more often defects created in a pair at a given time tend to annihilate with each other in the same pair at a subsequent time [26,30], which means that correlations between defects are important effects in their creation and annihilation dynamics and leads to a modified Poisson statistics in their number fluctuations [29]. A theoretical understanding of the effect of the self-induced mean flow on the collective statistical properties of defect motion is still lacking. However, experimentally measured velocity statistics during the spatiotemporal chaotic dynamics of uniaxial stripes in inclined layer convection are observed to be slightly anisotropic, and the exponents in the tail distribution of both climb and glide motion are close to -3 [13]. This is suggestive of a dynamical regime dominated by annihilations of dislocation pairs.

In this paper, we consider a simpler setup where nonrelaxational motion is driven by an externally imposed flow such that defects are constantly created and annihilated, leading to a statistically stationary defect dynamics. This can be attained in an anisotropic stripe system when a shear flow is acting normal to the stripe orientation. The role of the shear flow is different from the commonly studied case of shear alignment of isotropic stripes [13,31,32] or the buckling instability under shear acting along uniaxial stripes orientation [33].

The purpose of this paper is threefold: (i) to present an efficient numerical method for tracking the position and velocity of topological defects, (ii) its application to study the collective motion of dissipative vortices both in 2D and 3D and dislocations in 2D, and (iii) to report on numerical results where the anisotropic motion (glide and climb) of dislocations subjected to a simple shear flow is explicitly manifested in the velocity distributions, even though the statistics during phase ordering are similar to those corresponding to the isotropic motion of vortices.

To track the position and velocity of topological defects, we implemented a numerical method inspired by the analytical treatments of Halperin [34] and Mazenko [16]. The method was originally developed to locate defects in an $O(2)$-symmetric order parameter with a Ginzburg-Landau relaxation dynamics in 2D. We show numerically that this method works very well for Ginzburg-Landau dynamics both in 2D and 3D, and it is also suitable for tracking dislocations in systems controlled by anisotropic Swift-Hohenberg dynamics. Measuring the velocity statistics of vortices during relaxational dynamics, we find a universal inverse cubic tail for defects of the same codimension, that is, point vortices in 2D and vortex filaments in 3D. The scaling law is directly related to the pairwise interactions between vortices prior to annihilation and reconnection events (in 3D). Finite-size core effects induce a Gaussian cutoff to the v^{-3} scaling. A similar statistical behavior is observed in the velocity of dislocations in anisotropic stripe patterns. Despite the fact that dislocations are dominated by their transverse motion and thus are highly anisotropic, the distribution of the climb and glide velocities shows the same long tail behavior. In the presence of an external shear flow that leads to nonrelaxational dynamics, the motion anisotropy is explicitly manifested in different statistics of the velocity components. While the slow motion is highly influenced by the shear flow, the high-speed limit may still be dominated by the nearest-neighbor interactions.

The paper is organized as follows. Following this introduction, we proceed in Sec. II to discuss a method of efficiently tracking topological defects and apply it to a collection of vortices as well as ensembles of dislocations. Section III presents numerical results on the vortex velocity statistics in 2D and 3D simulations of phase ordering. We discuss the statistics of dislocations during phase ordering and nonrelaxation dynamics sustained by an external shear flow in Sec. IV. Concluding remarks and a summary are provided in Sec. V.

II. DEFECT DYNAMICS

Here we present a numerically efficient method for tracking codimension-2 topological defects. The method is applied to Ginzburg-Landau dynamics of vortices in 2D and 3D, as well as to Swift-Hohenberg dynamics of dislocations in 2D anisotropic stripes. The effect of hydrodynamic interactions in the presence of an external shear flow is discussed in the context of dislocation dynamics.

A. Locating and tracking defects

The identification and evolution of a large population of defects are generally nontrivial problems in systems described by continuum approaches. Moving from the field variables to the discrete particle variables is not straightforward. In most defect studies, one resorts to various approximate methods to estimate the locations and velocity of defects by following their trajectories [13,19,22].

In systems that can be described by an $O(2)$-symmetric order parameter $\psi(\boldsymbol{r},t)$ whose evolution depicts the ordering kinetics from an initially disordered state to an ordered state (either isotropic and homogeneous or a periodic pattern), one can use an elegant method based on a transformation from the order-parameter dynamics to the discrete defect dynamics. The analytical formulation of this method was pointed out first by Halperin [34] and was subsequently extended by Mazenko to determine the velocity of various topological defects [4,16,35,36]. To our knowledge, this method has not been previously implemented numerically. We show that it is an efficient numerical tool used for tracking the evolution of various types of defects.

The basic idea of this technique is that topological defects are located at the zeros of the complex order-parameter field $\psi(\boldsymbol{r},t)$ [34]. The transformation from field to particle variables is determined by the Jacobian determinant $\mathcal{D}(\boldsymbol{r}) = ||\partial\psi_n/\partial r_j||$, where $n = 1,2$ stands, respectively, for the real and imaginary components of the order-parameter field, i.e., $\psi = \psi_1 + i\psi_2$, and $j = 1,\ldots d$, with d being the spatial dimension. Thus, for $d = 2$, $\mathcal{D}(\boldsymbol{r})$ is a scalar quantity. Its sign determines the topological charge, i.e., $q = \mathcal{D}(\boldsymbol{r})/|\mathcal{D}(\boldsymbol{r})| = \pm 1$, and the charge density is given as

$$\rho(\boldsymbol{r},t) = \delta(\psi)\mathcal{D}(\boldsymbol{r},t) = \sum_{i=1}^{N} q_i \delta(\boldsymbol{r} - \boldsymbol{r}_i) \tag{1}$$

for a collection of N-point vortices. The extension to string defects in $d = 3$ is that the Jacobian determinant becomes a vector field $\mathcal{D}_j$(r) related to the vortex filament density by

$$\rho_j(\boldsymbol{r},t) = \delta[\psi(\boldsymbol{r},t)]\mathcal{D}_j(\boldsymbol{r}), \tag{2}$$

where the notation for the Dirac δ function is used [4].

The defect velocity $\boldsymbol{v}$ is determined from the property of topological defects that their total charge is conserved (defects are created and annihilated in pairs of opposite charge), namely,

$$\partial_t \rho + \nabla \cdot (\rho \boldsymbol{v}) = 0, \tag{3}$$

with the charge density $\rho(\boldsymbol{r},t)$ defined above. For example, in the case of point defects in 2D, the Jacobian determinant becomes $\mathcal{D} = 1/(2i)(\nabla_x\psi^*\nabla_y\psi - \nabla_x\psi\nabla_y\psi^*)$, where ψ^* is the complex conjugate of ψ. By differentiating $\mathcal{D}$ with time, a current $\boldsymbol{J}^{(\dot{\psi})}$ can be defined as [16]

$$\boldsymbol{J}_\alpha^{(\dot{\psi})} = -\frac{i\epsilon_{\alpha\beta}}{2}(\dot{\psi}\nabla_\beta\psi^* - \dot{\psi}^*\nabla_\beta\psi), \tag{4}$$

such that the $\mathcal{D}$ field satisfies the continuity equation

$$\partial_t \mathcal{D} + \nabla \cdot \boldsymbol{J}^{(\dot{\psi})} = 0. \tag{5}$$

Summation over repeated indices is implied, and $\epsilon_{\alpha\beta}$ is the two-dimensional antisymmetric tensor, $\epsilon_{xx} = \epsilon_{yy} = 0$ and $\epsilon_{xy} = -\epsilon_{yx} = 1$. From Eqs. (3) and (5), the defect velocity is determined as $\boldsymbol{v} = \boldsymbol{J}^{(\dot{\psi})}/\mathcal{D}$. The defect velocity depends on the dynamics of the order parameter through its time derivative $\dot{\psi}(\boldsymbol{r},t)$. Explicitly, the velocity components are given by

$$\begin{aligned} v_x &= -i\frac{\dot{\psi}\nabla_y\psi^* - \dot{\psi}^*\nabla_y\psi}{2\mathcal{D}}, \\ v_y &= i\frac{\dot{\psi}\nabla_x\psi^* - \dot{\psi}^*\nabla_x\psi}{2\mathcal{D}}, \end{aligned} \tag{6}$$

where ψ^* is the complex conjugate of the ψ field and $\dot{\psi}$ is the time derivative of ψ which determines the evolution of the order parameter. This can be generalized to $d = 3$, in which case the velocity of vortex filaments is calculated as [4]

$$\boldsymbol{v} = \frac{\boldsymbol{\mathcal{D}} \times (\dot{\psi}^*\nabla\psi - \dot{\psi}\nabla\psi^*)}{2\mathcal{D}^2}, \tag{7}$$

where $\mathcal{D}^2 = \sum_{j=1}^{3}\mathcal{D}_j\mathcal{D}_j$ and the velocity vector field is $\boldsymbol{v} = (v_x, v_y, v_z)$.

In the dilute defect density limit, it can be shown that the vortex velocity defined by Eq. (6) becomes a function of the phase and amplitude gradients of the order parameter ψ near the vortex core [35]. The formula is exact and applies equally well for a high density of defects.

B. Application to vortices

Vortices are defined as the zeros of an order parameter $\psi(\boldsymbol{x},t)$ with rotational symmetry (complex field) [2]. The fact that the complex field vanishes at the core of a defect is equivalent to a phase singularity; i.e., the phase of the order parameter varies discontinuously around a closed contour surrounding the defect. The phase θ is obtained from $\psi = |\psi|e^{i\theta}$. The shift in phase around the contour or the winding number, i.e., $\oint \nabla\theta \cdot d\boldsymbol{l} = 2\pi n$, defines the topological charge of the defect. A single vortex corresponds to a unit of topological charge, that is, $n = 1$.

We now consider the nonconservative evolution of a $\psi(\boldsymbol{r},t)$ field described by the time-dependent Ginzburg-Landau equation given by

$$\partial_t\psi = \nabla^2\psi + \psi(1 - |\psi|^2), \tag{8}$$

which we simulate both in 2D and 3D. For computational efficiency, we solve Eq. (8) by a cell dynamical system (CDS) algorithm, that was originally developed for studying spinodal decomposition dynamics [37] and extensively used to study phase ordering of systems with continuous symmetry [3,38,39]. In the Appendix we provide a detailed description and recapitulation of the algorithm, for completeness, and

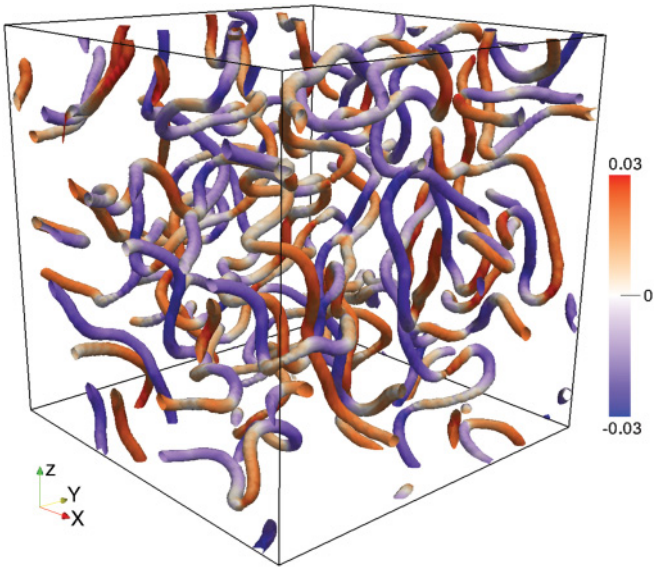

FIG. 1. (Color online) Snapshot of a measure of the charge-density vector field for a configuration of vortex filaments in 3D simulation of phase ordering. The figure shows the x component $\mathcal{D}_x$ of the Jacobian determinant defined in Sec. II. The system size in this simulation is 128^3.

define the parameters of the simulation used below. In particular, the depth of the quench corresponds to the parameter A, and the strengths of the diffusive couplings in the model are denoted by C. Simulations in 2D are done on a system size of 1024^2 cells, while in 3D we use 128^3 cells for $dx = 1$. Unless otherwise noted, the values for the CDS parameters A, the depth of the quench, and C, the strength of the spatial coupling, are $A = 1.5$, $C = 3/20(1 + A)$ (for 2D), and $C = 3/24(1 + A)$ (for 3D). Results were averaged over 48 random initial conditions, unless otherwise noted.

The vortex dynamics from the Ginzburg-Landau evolution in Eq. (8) is similar to the previous one reported in Ref. [22]. Here, we use a different tracking method for locating the defects and extend the analysis to vortex filaments in 3D.

A snapshot of the charge-density field for vortex filaments in 3D obtained using Halperin and Mazenko's method, discussed in the previous section, is shown in Fig. 1. The charge-density field is directly proportional to the $\mathcal{D}$ field, which is zero everywhere except along the vortex filaments. A similar representation is obtained for point vortices in 2D, where the charge field is localized at the vortex core and vanishes everywhere else, as shown in Fig. 2(a). Since the charge density is directly related to the $\mathcal{D}$ field, it means that the defect velocities are meaningfully defined only at the defect positions. In the numerical discretizations, defects are associated with small blobs (in 2D) or thin tubes (in 3D) with a specific characteristic size that defines the vortex core size. We define the defect regions as the locations at which the absolute charge density is above 75% of the theoretical value of $|q| = 1$. The values of the $\mathcal{D}$ field are finite within these regions, and thus the division is also finite. The velocity of the located defects is determined from Eq. (7) for filaments in 3D and Eq. (7) for point vortices in 2D. The time derivative

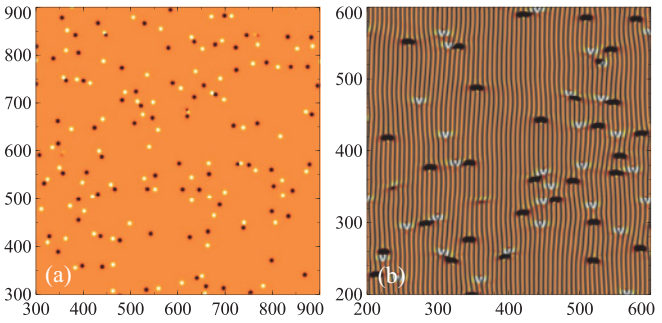

FIG. 2. (Color online) (a) Snapshot of the charge-density field corresponding to a configuration of point vortices in 2D simulations. In panel (b), we show the dislocations in an underlying anisotropic stripe configuration. The lighter blobs correspond to defects that have a positive charge, while the darker blobs are the defects of the opposite charge. The system size in both cases is 1024^2, while the snapshots are drawn from a subset.

$\dot{\psi}$ of the ψ field is defined by the right-hand-side expression in Eq. (8), namely, $\dot{\psi} \equiv \nabla^2\psi + \psi(1 - |\psi|^2)$.

C. Application to dislocations

Here, we focus on tracking dislocations in anisotropic stripe patterns. A similar tracking method can be extended to locate the defects in a crystal phase and will be the subject of a separate study reported elsewhere.

We consider the defects in a periodic pattern characterized by a preferred wave number $\boldsymbol{k}$ formed by stripes. Stripe patterns occur in a variety of systems, typical examples being convective rolls in Rayleigh-Bénard convection of isotropic fluids [5] and convective flows in nematic liquid crystals [40] in the dynamics of diblock copolymers [41]. When the orientation of the local ordering is random, as in isotropic stripes, we encounter both isolated defects such as dislocations or disinclinations as well as grain boundaries. The coexistence of different types of defects makes it difficult to analyze their statistics. Moreover, the ordering kinetics of isotropic stripes tends to be dominated at large times by grain-boundary slow motion, which can lead to glassy configurations [18]. By fixing the orientation of the stripes along a preferred axis, point defects such as dislocations can be isolated from the other types of defects. Examples of anisotropic stripes are in electrohydrodynamic convection of planary aligned liquid crystals [25] and Rayleigh-Benard convection of an inclined fluid layer [13].

The statistics of dislocations in anisotropic stripes has been discussed previously by Qian and Mazenko [23], who propose a model based on an effective Swift-Hohenberg (SH) free energy with an additional term that accounts for the coupling to an external field aligning the stripes along a preferred direction. The stripe pattern in 2D is represented by a real periodic field $u(\boldsymbol{r},t)$, which satisfies an anisotropic SH dynamics given by

$$\partial_t u = (1 - r|u|^2)u - (1 + \nabla^2)^2 u - c\nabla_x^2 u, \qquad (9)$$

where the last term is added to impose a preferred orientation of the stripes along the vertical y axis with $c > 0$ being the coupling strength to the external field. The quench depth $r > 0$ is interpreted in the context of convection patterns as

the deviation from the onset of convection, $r \approx R/R_c - 1$, where R is the Rayleigh number and R_c is the critical R at the onset [5]. The anisotropic preferred orientation can be seen by linearizing Eq. (9) around the mode solution $u \sim \exp(\omega t + ik_x x + ik_y y)$, with the growth rate obtained from Eq. (9) as

$$\omega = (1 - r) - \left(1 - k_x^2 - k_y^2\right)^2 + ck_x^2, \tag{10}$$

and imposing the condition $\omega(r;k_x,k_y) = 0$ at the onset of instability with respect to a mode of wave numbers k_x and k_y. The condition is found by minimizing ω with respect to k_x and k_y, i.e., $\partial\omega/\partial k_x = 0$ and $\partial\omega/\partial k_y = 0$. This leads to $k_y = 0$ and $k_x = \sqrt{1 + c/2}$ for $c > 0$.

We consider the amplitude formulation of Eq. (9) with an additional contribution due to an external shear flow. We impose a shear flow that is normal to the main orientation of the stripes to allow for the nucleation of defects due to wave-number shifts by shear deformation. In order to track dislocations in a complex order-parameter field, we write the periodic field in terms of its complex envelope field $\psi(\boldsymbol{r},t)$, namely, $u(\boldsymbol{r}) = \sqrt{r}\psi(\boldsymbol{r})e^{i\boldsymbol{k}\cdot\boldsymbol{r}} + \text{c.c.}$ Without loss of generality, we consider stripes with the wave vector parallel to the horizontal x axis, i.e., $\boldsymbol{k} = (k_0,0)$. The complex ψ field satisfies an amplitude equation derived from Eq. (9) and given to the leading order in r as

$$\partial_t\psi + \dot{\gamma}_x\mathcal{L}_x[\psi] = r(1 - |\psi|^2)\psi - \mathcal{L}^2[\psi] - c\mathcal{L}_x^2[\psi], \tag{11}$$

where $\mathcal{L} \equiv (\nabla^2 + 2i\boldsymbol{k}\cdot\boldsymbol{\nabla})$ is derived from $(1 + \nabla^2)$ and $\mathcal{L}_x \equiv \boldsymbol{\nabla}_x + ik_0$ comes from the gradient $\boldsymbol{\nabla}_x$. The advection term is determined by a velocity field, which hereby is taken as a simple shear flow $\dot{\boldsymbol{\gamma}} = v_0 y\hat{\boldsymbol{x}}$, and the last term is added to impose a preferred orientation of the stripes along the vertical y axis.

We integrate numerically Eq. (11) using a fourth-order Runge-Kutta scheme and a spherical approximation for the gradients [42] (see Appendix) on a square domain of size $1024dx \times 1024dx$. The time step is $dt = 0.05$ and the spatial resolution is $dx = \pi/4$, so that about eight grid points are used to resolve the pattern wavelength $\lambda = 2\pi/k_0$, with $k_0 = 1$. The other parameters are set to $c = 1$, $r = 1$, and v_0 is a changing parameter. In the absence of shear, period boundary conditions on all sides are used. At a finite shear rate, we impose zero flux boundary conditions on the upper and lower boundaries and periodic conditions on the lateral boundaries.

Dislocations are efficiently located as the zeros of the complex envelope field ψ using Mazenko's algorithm. In Fig. 2(b), we illustrate a stripe configuration with the location of dislocations and their topological charge proportional to the Jacobian determinant $||\partial\psi_n/\partial r_j||$. The velocity of dislocations is obtained using Eq. (6) with the evolution of the order parameter given by the right-hand side of Eq. (11), namely, $\dot{\psi} \equiv r(1 - |\psi|^2)\psi - \mathcal{L}^2[\psi] - c\mathcal{L}_x^2[\psi]$.

III. VORTEX STATISTICS

To determine the velocity statistics of vortices, we initiate the system in a disordered state and follow the ordering kinetics dominated by the initial formation and subsequent coarsening of topological defects. At a particular time, we calculate the local defect velocities $\boldsymbol{v}$ using Mazenko's method as described above. We save the absolute values, $v = |\boldsymbol{v}|$, every few time iterations and run the system from 48 random initial conditions. This way, we compute the probability distribution function (PDF) of the defect velocity at a given time, i.e., $F(v,t)$. In the asymptotic limit $t \to \infty$ of the coarsening dynamics, we expect scale invariance of the typical coarsening length scale, i.e., $L(t) \sim t^{1/2}$ for nonconservative dynamics (apart from logarithmic corrections in 2D). Hence the typical velocity obtained as $1/L(t)$ scales with time as $\langle v(t)\rangle \sim t^{-1/2}$ and corresponds to the velocity of defects in a pair prior to annihilation and separated by a distance of the order of $L(t)$. In the simulations, $\langle v(t)\rangle$ is the ensemble average velocity at a particular time, and when calculated over long times it converges to the expected asymptotic scaling. This dynamical scaling of the mean velocity implies also a scaling with time of $F(v,t)$. We notice that the time dependence in the PDFs can be eliminated by rescaling the velocity variables by their ensemble average values at a given time, i.e., $\tilde{v} \equiv v/\langle v(t)\rangle$. Analytically, this corresponds to the rescaling $F(v,t) = t^{1/2}P(vt^{1/2})$.

The scaling function $P(x)$ of the velocity distribution is a function of the rescaled velocity field $v/\langle v(t)\rangle$ and has a broad tail with an inverse cubic decay. This is shown in Fig. 3 for 2D simulations and Fig. 4 for 3D dynamics. The v^{-3} tail corresponds to the regime of large velocities obtained in pair interactions prior to annihilation events or, for 3D, also reconnections events. The -3 scaling exponent is determined by the logarithmic mutual interaction potential as shown in, e.g., Refs. [15,43]. Since point defects in 2D and filaments in 3D are both codimension-2 topological defects with the same type of interactions, we expect a similar scaling behavior. This

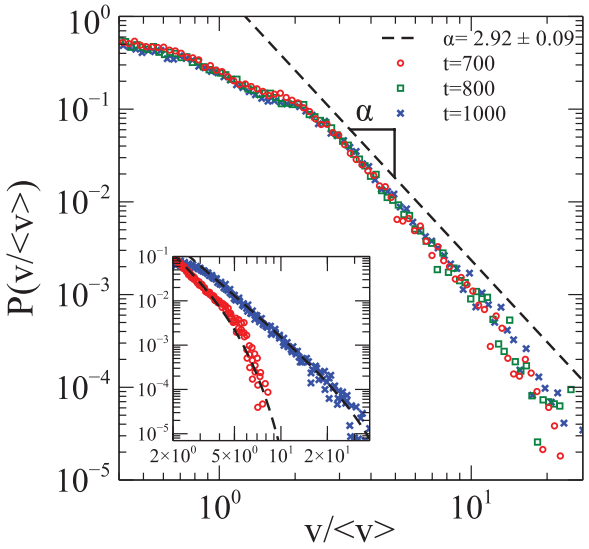

FIG. 3. (Color online) Collapsed probability distribution function (scaling function) of the absolute velocity of point vortices in 2D during phase ordering. (Inset) PDF of the defect velocity for different core sizes (open circles correspond to larger core size and crosses correspond to smaller core size) to show that the Gaussian cutoff depends effectively on the vortex core size. The model parameters for the inset figure are $A = 2.05$ (open circles), $A = 1.05$ (crosses), and $C = 3/20(1 + A)$. In the main graph, $A = 1.5$. Here $v \equiv |\mathbf{v}|$.

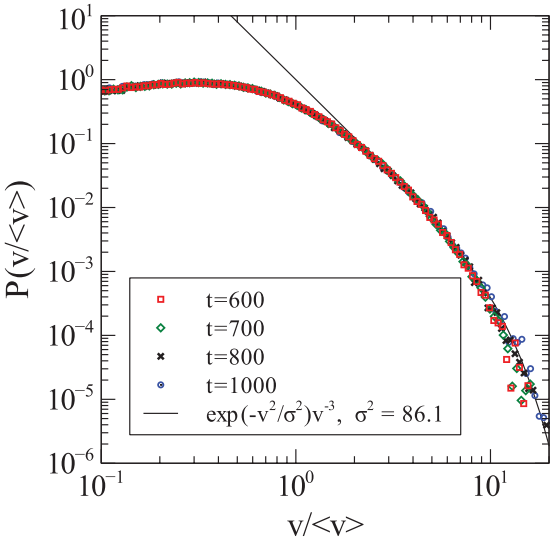

FIG. 4. (Color online) Scaling function of the probability distribution function of the absolute velocity of vortex filaments in 3D during phase ordering. Here $v \equiv |\mathbf{v}|$.

is consistent with other numerical studies that also show that the tail of the $P(v)$ distribution is dominated by the v^{-3} scaling both in 2D and 3D simulations [11,12]. We provide additional numerical evidence for this scaling regime also during phase ordering kinetics.

From Figs. 3 and 4, we notice that the vortex core structure has a drastic influence on the defect velocity statistics [43]. This effect is given by a Gaussian tail which takes over the v^{-3} regimes at very large fluctuations. The vortex core size is more pronounced in 3D simulations, due to numerical bounds on higher spatial resolutions. It is easier to vary the aspect ratio between system size and vortex core size in 2D simulations to observe the vortex core effect. In CDS simulations, the core size is fixed by the parameter A. We consider two different values of A, namely, $A = 1.05$ for small cores and $A = 2.05$ for larger cores, averaged over 2000 random initial conditions. The system size was reduced to 128^2 cells. The dependence of the Gaussian cutoff on the core size is shown in the inset of Fig. 3, while the velocity distribution for an intermediate core size, parametrized by $A = 1.5$, is plotted in the main graph of Fig. 3, using 1024^2 cells and averaging over 48 initial conditions.

IV. DISLOCATION STATISTICS

Next we discuss the statistics of dislocations in anisotropic stripes during phase ordering and nonrelaxational dynamics assisted by a shear flow.

A. Dynamical scaling regimes

In the early stages, the evolution of defects is dominated by pairwise interactions leading to annihilations and a decrease in the density of defects. We measure the density of defects $\rho_d(t)$ as the ratio between the effective area occupied by the defects and the total system area. Alternatively, the number of defects N can be estimated as the area occupied by the defects divided by the approximate core area of a defect. In simulations, we

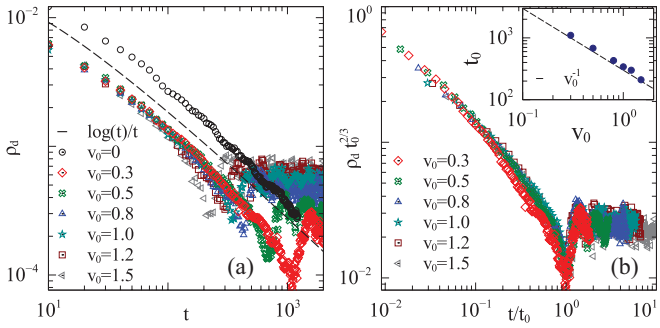

FIG. 5. (Color online) (a) Density of defects ρ_d as a function of time t for different values of the imposed shear velocity v_0. (b) Data collapse of the rescaled density with the mean density in the statistical steady state $\rho_0 \sim t_0^{-2/3}$, where t_0 is the crossover time to the steady state. The inset figure shows how t_0 scales with v_0 as $t_0 \sim 1/v_0$.

choose a large system size of 1024^2 and calculate $\rho_d(t)$ as a function of time, starting from a random initial condition. During the relaxation dynamics, the defect density for a very large system is equivalent to the averaged density over many initial conditions for a smaller system size and is a smooth function of time [44]. As expected in the coarsening regime, the density obeys a power law in time as $\rho_d(t) \sim \log(t)/t$ like the density of vortices in Ginzburg-Landau theory [22]. This behavior is shown in Fig. 5(a) by the data in the open circles and is consistent with formal arguments that the anisotropic Swift-Hohenberg dynamics can be mapped onto the isotropic Ginzburg-Landau dynamics [2]. In Fig. 5(a), we also plot the density $\rho_d(t)$ as a function of time for various values of the shear rate v_0. We notice that in the late stages, when long-range hydrodynamic interactions set in, the density of defects ceases to decrease monotonically and approaches instead a statistically steady state. In this steady state, the defect density fluctuates in time about a mean value because of the sporadic pair creations and subsequent annihilations of defect pairs. Averages over initial conditions would lead to a constant mean density ρ_0 in this steady state, i.e., $\langle \rho_d(t) \rangle_{IC} \to \rho_0$ as $t \to \infty$. We also observe that the mean number of defects $\langle N \rangle$ in the steady state appears to increase with the applied shear v_0, suggesting that the creation rate of defect pairs depends on v_0. Also, the mean-square fluctuations $\langle N^2 \rangle - \langle N \rangle^2$ in the number of defects increase monotonically with $\langle N \rangle$ with significant deviations from what would be expected in a Poisson process. It appears that the number statistics of defects behaves in a similar manner to that in defect turbulence [30], although a detailed analysis of this suggestion would be beyond the scope of this paper.

From the data presented in Fig. 5(b), we can determine the crossover time t_0 to the statistical steady state, and we find that it increases to a first approximation as $t_0 \sim v_0^{-1}$, as shown in the inset of Fig. 5(b). It turns out that phase ordering assisted by hydrodynamic effects slows down the growth of the typical distance between defects with corrections that follow a $L(t) \sim t^{1/3}$ law until saturating to the steady state. This implies that the steady-state defect density can be estimated as $\rho_0 \sim L(t_0)^{-2} \sim t_0^{-2/3}$. Equivalently, the mean density in the steady state increases with the applied shear as $\rho_0 \sim v_0^{2/3}$. As a first step to see whether there is any data collapse associated

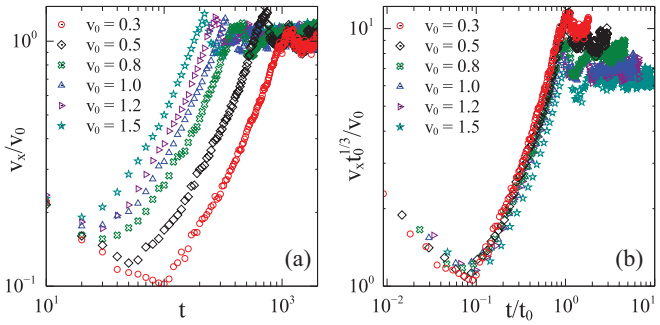

FIG. 6. (Color online) (a) Evolution with time of the ensemble average of the velocity component $v_x \equiv \langle |v_x(t)| \rangle$ for different values of the shear rate. (b) Data collapse of the rescaled v_x as a function of the rescaled time t/t_0.

with this scaling behavior, we plot the rescaled ρ/ρ_0 versus the rescaled t/t_0 as shown in Fig. 5(b).

Because the normal stripes are aligned along the y direction, the climb and glide motions of the dislocations correspond, respectively, to the vertical and horizontal velocities. The motion is anisotropic and dominated by the transverse (gliding) dynamics of dislocations. We observe that climb motion typically occurs when two dislocations of opposite topological charge approach each other to annihilate; otherwise, dislocations would move by gliding across the stripes. Nevertheless, when the two motions are driven by the local pairwise interactions between dislocations, they exhibit similar characteristics. In the early states, where the dynamics is controlled mainly by the phase ordering and annihilations of dislocations, the ensemble average of the net velocities (absolute values), $\langle |v_x| \rangle(t)$ and $\langle |v_y| \rangle(t)$, scale with time as $t^{-1/2}$ until hydrodynamic effects set in and the defects are accelerating until they cross over at t_0 to a statistically stationary state. This behavior is shown in Fig. 6(a) for $\langle |v_x| \rangle$ and in Fig. 7(a) for $\langle |v_y| \rangle$, corresponding to different values of the imposed shear velocity v_0. In the later stages, hydrodynamic effects become important and there is a transient regime where the mean velocities increase almost linearly with time until t_0, after which a statistically stationary state is reached. Since we run large-scale simulations for a given realization without averaging over initial conditions, the ensemble-averaged velocities, $\langle |v_x| \rangle(t)$ and $\langle |v_y| \rangle(t)$, correspond to time series in the statistical steady state. Averaging these fluctuations over many initial conditions

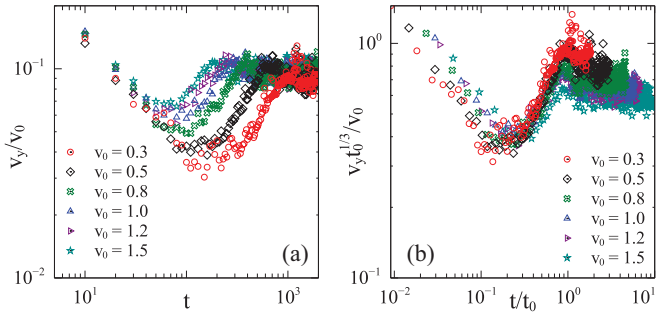

FIG. 7. (Color online) (a) Evolution with time of the ensemble average of the velocity component $v_y \equiv \langle |v_y(t)| \rangle$ for different values of the shear rate. (b) Rescaled v_y plotted as a function of the rescaled time t/t_0.

would smooth out the late-stage time dependence to a constant value.

The mean-square fluctuations in the steady state are an increasing function of the applied shear. We observe that the mean value of the climb velocity is approximately an order of magnitude smaller than the typical velocity of gliding. A rescaling of velocity components as a function of the rescaled time in the units of t_0 is presented in Figs. 6(b) and 7(b), which however gives a poor data collapse. Improving this turned out to be a challenging task, one of the reasons being that there is an additional characteristic time scale given by the crossover from the relaxation dynamics to the transient period of acceleration prior to the steady state. It may be that this time scale also plays a role in the scaling function, but we have not succeeded in including it to our satisfaction. This is an unresolved issue that deserves a separate detailed study.

The statistically stationary regime is characterized by fluctuations in the density of defects and their velocities around a mean value that depends on the imposed shear flow. Fluctuations in the defect density are attributed to the sudden nucleation of dislocation pairs and their subsequent annihilation, either with the same pair member or with dislocations from another pair.

Physically, the nucleation mechanism is related to the phase shifts induced by the transverse shear deformations. The reason for this is that the action of an external shear flow is cumulative in the phase θ of the complex envelope field $\psi = |\psi| e^{i\theta}$ and its gradients $\nabla\theta$, similar to the effect of the self-induced mean flow [45]. The shear flow advects the underlying stripe pattern together with its defects. This motion induces small undulations along the stripes which build up stresses and create distortions in the pattern. These distortions, which are localized into transverse "shear bands," grow with time up to the point where they locally tear apart the stripes, releasing pairs of defects. The shear flow affects both the isolated motion of defects and, more importantly, the interaction between defects. The effect of the large-scale flow on the defect interactions becomes stronger where the defect motion is slower [45].

B. Velocity statistics

In the absence of shear flow, the motion of dislocations is symmetric. Although the mean velocity in the absolute value is nonzero and related to the mutual interaction forces, the velocity of dislocations averages out to zero. This is equivalent to the symmetric probability distributions of the velocity fluctuations, as shown in Fig. 8. The actual distribution is time dependent due to quench dynamics by annihilations. However, using the dynamical scaling behavior of the probability distribution we can remove the time dependence by effectively rescaling the dislocation velocity by the ensemble average of the absolute velocity at a given time, i.e., $\tilde{v}_i \equiv v_i/\langle |v_i(t)| \rangle$, with $i = x, y$ for the two components. The distribution of these rescaled velocities corresponds to the scaling function of the time-dependent probability distribution, as discussed previously in the context of vortex dynamics. From Fig. 8, we notice that the probability distributions of the climb and glide velocities retain a similar form that is characterized by a long tail with a -3 power law, as in the relaxational dynamics of vortices. This is consistent with previous numerical studies

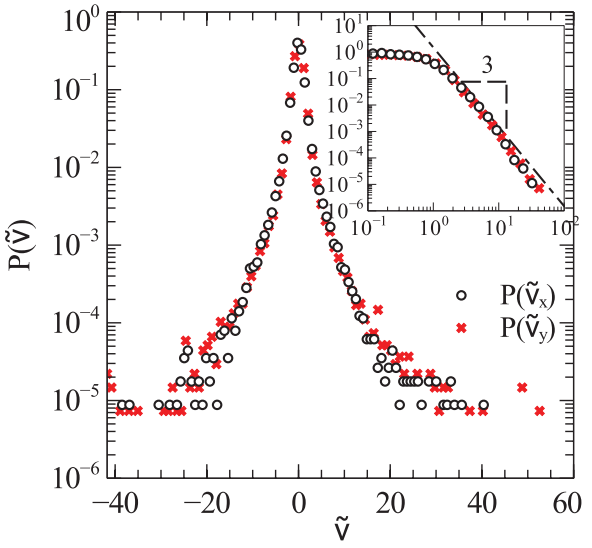

FIG. 8. (Color online) Time-independent scaling function of the probability distribution corresponding to climb (crosses), respectively glide (open circles) velocities during the phase ordering in the absence of an external field. The rescaled velocity variable is given as $\tilde{v}_j \equiv v_j/\langle|v_j|\rangle$ for $j = x, y$. The inset figure shows the log-log plot of the PDF calculated with logarithmic binning.

of the velocity statistics of defects in the anisotropic Swift-Hohenberg dynamics from Ref. [23].

At a finite shear rate and in the late stage of a statistically stationary regime, the motion of dislocations is influenced by the imposed flow. Dislocations of opposite topological charges tend to move in opposite directions, with an asymmetry in their mean transverse motion that is related to the shear rate, i.e., $\dot{\gamma} \sim (\langle v_x^+\rangle - \langle v_x^-\rangle)$, while the climb motion remains almost symmetric. The velocity probability distribution for positive, respectively, negative, dislocations becomes the same when we rescale their corresponding absolute velocities as $\tilde{v}^s \equiv |v^s|/\langle|v^s|\rangle$, where $s = \pm$, so that $P^+(\tilde{v}^+) = P^-(\tilde{v}^-)$.

In Fig. 9, we plot the probability distribution functions of the rescaled gliding velocities and climbing velocities in the steady-state regime. For the transverse motion, the small-scale velocity fluctuations are normally distributed around the mean flow. Large fluctuations against the flow are due to events where pairs of dislocations of opposite charge, gliding opposite to their drift flow, are attracting and annihilating. These events contribute to the long left tail for $P^+(v_x)$ and right tail for $P^-(v_x)$. The statistics of small climb velocities are also influenced by the imposed shear flow and given by the slight asymmetry in the $P^s(v_y)$. However, the large fluctuations in the longitudinal motion are due to pair interactions prior to annihilations. These fluctuations are captured by the long tails in the $P(v_y)$ distribution and they seem to follow the inverse cubic law, but with less accuracy than in the relaxational case. Typically, a nucleation event leads to a burst in the local density of dislocations which will annihilate subsequently by the fast climbing motions. However, these large velocity events occur on a longer time scale than during relaxational dynamics, so that the system needs to be followed longer in the steady state. This is computationally challenging, because of the prior

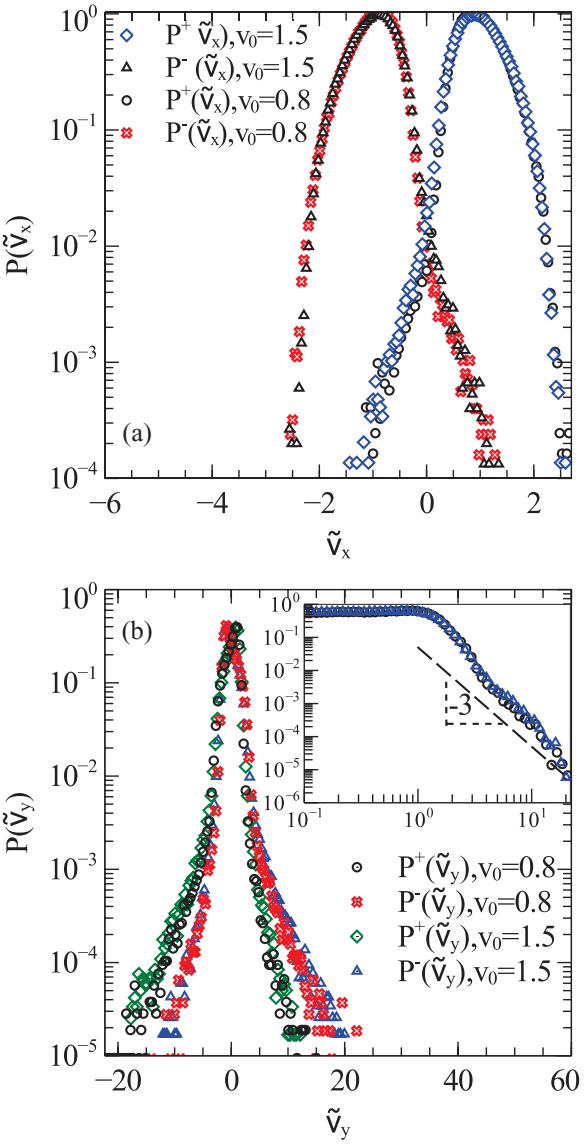

FIG. 9. (Color online) (a) PDF of the gliding velocity for positive (open diamonds and circles) and negative (open triangles and crosses) dislocations in the statistically stationary state at different shear rates. (b) Probability distribution function of the climb velocity for positive (open circles and diamonds) and negative (open crosses and triangles) dislocations in the statistically stationary state. In both cases, the rescaled velocity variable is $\tilde{v}_j \equiv v_j/\langle|v_j|\rangle$ for $j = x, y$. The inset figure shows the log-log plot of the tail PDF with logarithmic binning.

transient acceleration period whose length increases as the driving force is decreased.

V. CONCLUSIONS

In summary, our numerical simulations suggest that the velocity statistics of codimension-2 defects exhibits a dynamical scale invariance with a scaling function that has a universal inverse cubic tail when the defect dynamics is driven by mutual pair interactions leading to annihilations. This is valid both for point defects in 2D and defect filaments in 3D during phase ordering kinetics. Finite-size effects of the defect core introduce a Gaussian cutoff to the v^{-3} scaling. A similar

statistical behavior is observed in the velocity of dislocations in anisotropic stripe patterns during phase ordering. Although the motion is highly anisotropic and dominated by the gliding of dislocations, the distributions of the climb and glide velocity fluctuations exhibit the same algebraic tail when the motion is driven by the local interactions between dislocations. During nonrelaxational dynamics assisted by an external transverse shear flow, small velocity fluctuations are influenced by the mean flow, whereas the asymptotically large fluctuations are still due to pairwise interactions. In statistically stationary dynamics, anisotropic defect motion is manifested also in anisotropic statistics of the glide and climb velocities. In this study, we have neglected the effect of a self-induced mean flow in the defect dynamics. This effect is, however, important to capture the spatiotemporal chaotic dynamics, as seen from experiments. It would thus be interesting to study in future investigations the statistical properties of interacting defects when the combined effect of a large-scale flow and a self-induced mean flow is taken into account.

ACKNOWLEDGMENTS

This work is partially supported by the Center for Physics of Geological Processes at University of Oslo and by the US National Science Foundation Grant No. DMR 1044901.

APPENDIX: CALCULATION OF DERIVATIVES IN CELL DYNAMICAL SYSTEMS MODELS

We solve the time-dependent real Ginzburg-Landau dynamics from Eq. (8) using the cell dynamical systems approach (CDS) [38,39,46]. Numerical efficiency becomes particularly important in 3D simulations, and this method is tailored to that. The complex variable $\psi(\boldsymbol{r},t)$ is replaced by a $\psi_{i,j}^{(n)}$ (or $\psi_{i,j,k}^{(n)}$ in 3D) defined on a square lattice of size $N \times N$ (a cube of size $N \times N \times N$ in 3D) at time n. The idea of the CDS method is to construct a discrete set of maps for each lattice cell such that the flow properties of the continuous dynamical system are preserved. A cell dynamics is defined by two steps: a local update,

$$\tilde{\psi}^{(n+1)} = \frac{A\psi^{(n)}}{\sqrt{1+\psi^{2(n)}(A^2-1)}}, \tag{A1}$$

where $A > 1$ is a parameter that determines the global rate of convergence to the fixed points of the local double-well potential, and a global update taking into account the interactions between neighboring cells:

$$\psi^{(n+1)} = \tilde{\psi}^{(n+1)} + C\nabla^2\tilde{\psi}^{(n+1)}, \tag{A2}$$

where C is a constant proportional to the phenomenological diffusion constant. The isotropy of the order parameter being simulated naturally mandates the isotropy of the difference operators used to implement the coupled maps (see Tomita [42]). Oono and Puri [46] chose a nine-point stencil to implement a "Laplacian" operator, which is highly isotropic for a 2D square lattice [47]. This stencil reads

$$\nabla^2\psi \equiv \frac{3}{dx^2}\left(\frac{1}{6}\sum_{\mathrm{NN}}\psi + \frac{1}{12}\sum_{\mathrm{NNN}}\psi - \psi\right), \tag{A3}$$

where NN stands for the nearest neighbors in the discretized lattice and NNN are the next-to-nearest neighbors for each node in the lattice.

Considering the same isotropy requirements, the discretization of the 3D Laplace operator reads as [39]

$$\nabla^2 f \equiv \frac{3}{dx^2}\left(\frac{1}{9}\sum_{\mathrm{NN}}\psi + \frac{1}{36}\sum_{\mathrm{NNN}}\psi - \psi\right). \tag{A4}$$

Since the calculation of the position and velocities of defects involves first-order spatial derivatives of the ψ field, an isotropic discretization of the gradients is important in order to reduce the underlying lattice anisotropic effects. We use the isotropic version of the gradients both in 2D and 3D. Following the idea that these operators have to be accurately represented in Fourier space [47], we use the following stencil for 2D:

$$\begin{aligned}\nabla_x\psi \equiv \frac{1}{8dx}&(\psi_{i+1,j+1} + 2\psi_{i,j+1} - \psi_{i-1,j+1} \\ &+ \psi_{i+1,j-1} - 2\psi_{i,j-1} - \psi_{i-1,j-1}),\end{aligned} \tag{A5}$$

where i and j are the lattice indices for the x and y directions, respectively. Swapping indices we can obtain the corresponding expression for $\nabla_y\psi$. We note that this expression looks very similar to a four-point first derivative in a 2D square lattice [48]. For the gradients in 3D, the stencil reads

$$\begin{aligned}\nabla_x\psi = \frac{1}{8dx}&(\psi_{i+1,j+1,k} - \psi_{i-1,j+1,k} + \psi_{i+1,j-1,k} - \psi_{i-1,j-1,k} \\ &+ \psi_{i+1,j,k+1} - \psi_{i-1,j,k+1} + \psi_{i+1,j,k-1} - \psi_{i-1,j,k-1}) \\ &+ \frac{1}{4dx}(\psi_{i,j+1,k} - \psi_{i,j-1,k} + \psi_{i,j,k+1} - \psi_{i,j,k-1}),\end{aligned} \tag{A6}$$

with the corresponding index swap to obtain $\nabla_y\psi$ and $\nabla_z\psi$.

[1] I. Aranson and L. Kramer, Rev. Mod. Phys. **74**, 99 (2002).
[2] L. Pismen, *Vortices in Nonlinear Fields: From Liquid Crystals to Superfluids, from Non-Equilibrium Patterns to Cosmic Strings*, International Series of Monographs on Physics, Vol. 100 (Oxford University Press, New York, 1999).
[3] A. Bray, Adv. Phys. **51**, 481 (1994).
[4] G. F. Mazenko, Phys. Rev. E **59**, 1574 (1999).
[5] E. Bodenschatz, W. Pesch, and G. Ahlers, Annu. Rev. Fluid Mech. **32**, 709 (2000).
[6] I. Groma and B. Bakó, Phys. Rev. B **58**, 2969 (1998).
[7] M. Miguel, A. Vespignani, S. Zapperi, J. Weiss, and J. Grasso, Nature (London) **410**, 667 (2001).
[8] M. S. Paoletti and D. Lathrop, Annu. Rev. Condens. Matter Phys. **2**, 213 (2011).

[9] M. S. Paoletti, M. E. Fisher, K. R. Sreenivasan, and D. P. Lathrop, Phys. Rev. Lett. **101**, 154501 (2008).
[10] A. C. White, C. F. Barenghi, N. P. Proukakis, A. J. Youd, and D. H. Wacks, Phys. Rev. Lett. **104**, 075301 (2010).
[11] H. Adachi and M. Tsubota, Phys. Rev. B **83**, 132503 (2011).
[12] P. D. Ispánovity, I. Groma, G. Gyorgyi, F. F. Csikor, and D. Weygand, Phys. Rev. Lett. **105**, 085503 (2010).
[13] K. E. Daniels and E. Bodenschatz, Chaos **13**, 55 (2003).
[14] P. H. Chavanis and C. Sire, Phys. Rev. E **62**, 490 (2000).
[15] A. J. Bray, Phys. Rev. E **55**, 5297 (1997).
[16] G. F. Mazenko, Phys. Rev. Lett. **78**, 401 (1997).
[17] P. D. Ispánovity, I. Groma, G. Györgyi, P. Szabó, and W. Hoffelner, Phys. Rev. Lett. **107**, 085506 (2011).
[18] D. Boyer and J. Viñals, Phys. Rev. E **65**, 046119 (2002).
[19] D. Boyer, Phys. Rev. E **69**, 066111 (2004).
[20] W. Pesch and U. Behn, in *Evolution of Spontaneous Structures in Dissipative Continuous Systems*, edited by F. Busse and S. Müller, Lecture Notes in Physics Monographs (Springer, Berlin, 1998), Vol. 55, pp. 335–383.
[21] K. E. Daniels and E. Bodenschatz, Phys. Rev. Lett. **88**, 034501 (2002).
[22] H. Qian and G. F. Mazenko, Phys. Rev. E **68**, 021109 (2003).
[23] H. Qian and G. F. Mazenko, Phys. Rev. E **73**, 036117 (2006).
[24] H. S. Greenside, M. C. Cross, and W. M. Coughran Jr., Phys. Rev. Lett. **60**, 2269 (1988).
[25] I. Rehberg, S. Rasenat, and V. Steinberg, Phys. Rev. Lett. **62**, 756 (1989).
[26] C. Beta, A. Mikhailov, H. Rotermund, and G. Ertl, Europhys. Lett. **75**, 868 (2006).
[27] L. Gil, J. Lega, and J. L. Meunier, Phys. Rev. A **41**, 1138 (1990).
[28] M. Kaiser, W. Pesch, and E. Bodenschatz, Physica D **59**, 320 (1992).
[29] M. Hildebrand, M. Bär, and M. Eiswirth, Phys. Rev. Lett. **75**, 1503 (1995).
[30] C. Huepe, H. Riecke, K. Daniels, and E. Bodenschatz, Chaos **14**, 864 (2004).
[31] K. Song, Z. Sun, and L. An, J. Chem. Phys. **130**, 124907 (2009).
[32] V. Kumaran and D. S. S. Raman, Phys. Rev. E **83**, 031501 (2011).
[33] A. Zilman and R. Granek, Eur. Phys. J. B **11**, 593 (1999).
[34] B. Halperin, in *Physics of Defects, Proceedings of the Les Houches Summer School, Session XXXV*, edited by R. Balian, M. Kleman, and J.-P. Poirier (North-Holland, Amsterdam, 1981), pp. 814–857.
[35] G. F. Mazenko, Phys. Rev. E **64**, 016110 (2001).
[36] H. Qian and G. F. Mazenko, Phys. Rev. E **68**, 021109 (2003).
[37] Y. Oono and S. Puri, Phys. Rev. Lett. **58**, 836 (1987).
[38] M. Mondello and N. Goldenfeld, Phys. Rev. A **42**, 5865 (1990).
[39] M. Mondello and N. Goldenfeld, Phys. Rev. A **45**, 657 (1992).
[40] M. Zapotocky, P. M. Goldbart, and N. Goldenfeld, Phys. Rev. E **51**, 1216 (1995).
[41] J. J. Christensen and A. J. Bray, Phys. Rev. E **58**, 5364 (1998).
[42] H. Tomita, Prog. Theor. Phys. **85**, 47 (1991).
[43] I. Min, I. Mezić, and A. Leonard, Phys. Fluids **8**, 1169 (1996).
[44] A. Shinozaki and Y. Oono, Phys. Rev. E **48**, 2622 (1993).
[45] L. Pismen, Physica D **61**, 217 (1992).
[46] Y. Oono and S. Puri, Phys. Rev. A **38**, 434 (1988).
[47] P. I. C. Teixeira and B. M. Mulder, Phys. Rev. E **55**, 3789 (1997).
[48] M. Abramowitz and I. A. Stegun, *Handbook of Mathematical Functions with Formulas, Graphs, and Mathematical Tables* (Dover, New York, 1970), pp. 875–924.